Global estimates of mesoscale vertical velocity near 1000 m from Argo observations

Katy M. Christensen[1], **Alison R. Gray**[1], **and Stephen C. Riser**[1]

[1]School of Oceanography, University of Washington, Seattle, WA, USA

Key Points:

- Five-day averaged vertical velocities from Argo observations near 1000 dbar are non-normally distributed, with a high peak and heavy tails..
- Mesoscale vertical velocities are on the order of centimeters per day, but high-magnitude events can be on the order of meters per day.
- Vertical velocities estimated from Argo floats are spatially variable and correlated with topographic features and horizontal surface flow.

Corresponding author: Katy M. Christensen, katyc4@uw.edu

Abstract

Global estimates of mesoscale vertical velocity remain poorly constrained due to a historical lack of adequate observations on the spatial and temporal scales needed to measure these small magnitude velocities. However, with the wide-spread and frequent observations collected by the Argo array of autonomous profiling floats, we can now better quantify mesoscale vertical velocities throughout the global ocean. We use the underutilized trajectory data from the Argo array to estimate the time evolution of isotherm displacement around a float as it drifts at 1000 dbar, allowing us to quantify vertical velocity averaged over approximately 4.5 days for that pressure level. The resulting estimates have a non-normal, high-peak, and heavy-tail distribution. The vertical velocity distribution has a mean value of $(1.9 \pm 0.02) \times 10^{-6}$ m s^{-1} and a median value of $(1.3 \pm 0.2) \times 10^{-7}$ m s^{-1}, but the high-magnitude events can be up to the order of 10^{-4} m s^{-1}, We find that vertical velocity is highly spatially variable and is largely associated with a combination of topographic features and horizontal flow. These are some of the first observational estimates of mesoscale vertical velocity to be taken across such large swaths of the ocean without assumptions of uniformity or reliance on horizontal divergence.

Plain Language Summary

Vertical velocity in the ocean is a fundamental part of how water circulates throughout the globe. This impacts the temperature, salt, nutrients, and currents that make up the ocean. However, vertical velocities are very small and are, therefore, difficult to measure. In particular, the vertical velocities of ocean events that occur on roughly a weekly to monthly time scale (mesoscale) are poorly understood. We have developed a method for estimating these mesoscale vertical velocities across the globe using an array of autonomous robots called Argo floats. Our results show that vertical velocities vary greatly depending on location, with the largest values occurring where there is a combination of relatively shallow ocean depths and larger horizontal velocities. These estimates are some of the first of their kind to be made from observations across such large swaths of the ocean.

1 Introduction

An essential component of many physical, chemical, and biological processes, vertical motion in the ocean occurs at all spatial and temporal scales, with a high degree of variability in both. As the pathway from the ocean interior to the surface, vertical flow directly impacts thermocline structure, nutrient transport, and global circulation (Sverdrup, 1947; Stommel & Arons, 1959; Munk, 1966; Martin & Richards, 2001; Pilo et al., 2018; Liang et al., 2017). At the largest scales, the highly idealized model created by Stommel and Arons (1959) first estimated vertical velocities ranging between 0.5 and 3.0×10^{-7} m s^{-1}, averaged over large areas of the deep ocean, to compensate for dense water formation at high latitudes. As the spatio-temporal scale of the motions decrease, the magnitude of the associated vertical velocities tends to increase, as well as the variability across regions. The time-averaged vertical velocity at mid-depths associated with mesoscale motions has been estimated to be on the order of 10^{-6} m s^{-1} in a model (Liang et al., 2017), while values on the order of 10^{-4} m s^{-1} have been estimated within coherent vortices (Martin & Richards, 2001; Pilo et al., 2018). Small-scale vertical velocities observed at mid-depths within internal waves and lee waves have been estimated to be on the order of 10^{-2} m s^{-1} (Merckelbach et al., 2010) and 10^{-1} m s^{-1} (Cusack et al., 2017), respectively. While these smaller-scale estimates are often inferred from observations at the locations and depths where phenomena at these scales occur, estimates at meso and larger scales are commonly determined from numerical models which do not resolve the small-scale processes, horizontally or vertically. Directly observing vertical velocities in the ocean at these

scales has been an enduring challenge, due to the small magnitudes and high spatio-temporal variability (Stommel & Arons, 1959; Martin & Richards, 2001; Liang et al., 2017).

Despite the inherent difficulties, estimates of vertical velocities have previously been computed using observations across different scales, depths, and geographic locations, from many different sources including hydrographic profiles (Stommel & Arons, 1959; Munk, 1966; Martin & Richards, 2001), moorings (Sévellec et al., 2015), floats (Freeland, 2013; Cusack et al., 2017), and gliders (Merckelbach et al., 2010; Frajka-Williams et al., 2011). However, these estimates are often only able to capture either large- or small-scale vertical velocities due to limited sampling area or necessary assumptions of uniformity in depth and across smaller scales (Stommel & Arons, 1959; Freeland, 2013; Liang et al., 2017). The vertical velocities of mesoscale phenomena, which have horizontal scales of ∼100 km, are not particularly well observed, even though such motions are in one of the most dynamic energy bands in the ocean (Ferrari & Wunsch, 2009). Because mid-depth mesoscale velocities - both horizontal and vertical - are historically poorly characterized from observations, constraints on these flows in numerical models are completely lacking (Zilberman et al., 2023). Oceanic models such as those used for coupled climate projections may therefore be misrepresenting these vertical motions and the associated fluxes of tracers. To advance our understanding of this critical component of the oceanic velocity field, a novel approach is needed to greatly expand our ability to estimate vertical velocities in the global ocean from observations.

The observations collected by the Argo array of profiling floats constitute the largest global, open-ocean, subsurface oceanic dataset. Since the late 1990s, the Argo program has vastly increased the coverage and quality of oceanographic observational data (Roemmich et al., 2019). The classic Argo float cycle consists of a descent to 1000 dbar, a drift with the flow at that level in a quasi-isobaric fashion for approximately 10 days, another descent to 2000 dbar, an ascent to the surface while taking profile measurements of conductivity, temperature, and depth (CTD), and finally the transmission of data collected during the cycle to data acquisition centers using Iridium communications. The profile data from 0 to 2000 dbar are well-organized by the Argo program, comprehensively quality controlled, and have been extensively used in oceanographic research (Riser et al., 2016; Roemmich et al., 2019; Wong et al., 2020). Argo float profiles have previously been used to estimate vertical velocities in the open northeast Pacific (Freeland, 2013); however, that large-scale bulk estimate relied on computing the divergence within a well-defined control volume. Expanding this method to retrieve global vertical velocities at a finer scale, across a wide range of dynamic regimes, would require consideration of further processes and flows with the resulting uncertainties quickly dominating the estimates.

In addition to the profiles of temperature and salinity collected at the end of each cycle, a large number of Argo floats also record temperature and pressure measurements during the drift at 1000 dbar. The vast majority of floats do not measure salinity during the park phase. The temperature and pressure park phase data have been less frequently utilized than the profile measurements, and the associated quality control has been less consistent across platforms. Drift data at hourly resolution have previously been used to compute high-frequency isotherm displacement relative to the quasi-isobaric float, in order to examine internal wave characteristics near 1000 dbar (Hennon et al., 2014). The observations recorded during the drift phase of Argo floats remain, however, relatively untapped as a source of information about the subsurface ocean. The work presented here uses these data to estimate mesoscale ($\sim$ 5-day mean) vertical velocities at mid-ocean depths. The resulting near-global picture of the vertical flow at 1000 dbar, quantified directly from observations for the first time at such scales, not only reveals important patterns of spatial variability but also provides a critical benchmark for the subsurface flow in numerical models.

Section 2 introduces the analysis framework underlying the method we have developed to estimate vertical velocity using data recorded during an Argo float's drift phase.

In section 3 we apply the theory to the global Argo database and detail the extensive quality control steps that we have taken to ensure consistency in our estimates. The resulting vertical velocity estimates are presented in section 4, and several key geographic areas are highlighted. Additionally, we investigate how our estimates of vertical velocity relate to geographic location, bathymetry, horizontal flow, and sea level anomaly. Finally, section 5 compares the Argo-based estimates to model-based vertical velocities and discusses the implications of our results.

2 Theoretical Framework

To develop a method for estimating vertical velocity from high-frequency data recorded during the drift of Argo floats, we start with the evolution of temperature T following a water parcel

$$\frac{DT}{Dt} = k_z \frac{\partial^2 T}{\partial z^2} + k_h\left(\frac{\partial^2 T}{\partial x^2} + \frac{\partial^2 T}{\partial y^2}\right) + Q \tag{1}$$

where $k_z \frac{\partial^2 T}{\partial z^2}$ represents the rate of change in temperature due to vertical mixing including the vertical diffusivity k_z, $k_h(\frac{\partial^2 T}{\partial x^2} + \frac{\partial^2 T}{\partial y^2})$ represents the rate of change in temperature due to horizontal mixing including the horizontal diffusivity k_h, and Q corresponds to the rate of change in temperature from external sources and sinks of heat. Consider now the temperature evolution of a water parcel at mid-depths in the open ocean, over approximately 5 days. For the associated space and time scales, we can assume that the influence of horizontal mixing on temperature (following a water parcel) is negligible. In addition, if the vertical temperature gradient $\frac{dT}{dz}$ is constant, the contribution of vertical mixing will vanish. Thus, given these conditions are upheld, we can neglect the temperature change due to mixing altogether.

In the open ocean there are negligible sources and sinks of heat at the float parking depth of 1000 dbar, so we can also approximate Q as zero. Thus, we are left with $\frac{DT}{Dt} \approx 0$, which can be expanded to show the contribution due to advection by both horizontal and vertical velocities (u_H and w, respectively),

$$\frac{\partial T}{\partial t} + u_H \cdot \nabla_H T + w\frac{\partial T}{\partial z} \approx 0. \tag{2}$$

Applying this framework now to an ideal, completely isobaric float that perfectly follows the horizontal projection of the flow causes the horizontal velocity relative to the float, u_H, to vanish. In other words, the temporal evolution of temperature observed by the float as it is drifting with the horizontal flow will solely reflect the vertical advection of the background temperature gradient. Further decomposing the temperature into a time-averaged mean $\bar{T}$ and a time-varying anomaly T' and assuming that the temperature gradient at depth is constant at these spatial and temporal scales allows Equation (2) to be solved for w as

$$w = -\frac{\partial(T' + \bar{T})}{\partial t} \Big/ \frac{\partial T}{\partial z} \approx -\frac{d}{dt}\left(T' \Big/ \frac{\partial T}{\partial z}\right). \tag{3}$$

Thus, vertical velocity at the park depth can be computed from the observed rate of change of isotherm displacement relative to the float.

Moving from a theoretical particle to a real world float, we must consider that the float is not perfectly isobaric. In fact, the floats move on equilibrium surfaces defined by their mass, which deviate from pressure surfaces depending on surrounding conditions and float compressibility (Swift & Riser, 1994). Following Hennon et al. (2014), we account for the vertical motion of an Argo float away from the 1000-dbar isobar by subtracting the float displacement, given by the pressure anomaly during the drift. Doing this ensures that the isotherm displacement we estimate is a product of fluid motion alone.

We then incorporate the pressure correction term into Eq.3. The pressure measured by a float must also be converted into units of depth to give velocity in m s^{-1}, which can be done by assuming a hydrostatic balance ($z = \frac{P}{\rho g}$). Following this we are left with the following equation for w:

$$w = -\frac{1}{\rho g}\frac{d}{dt}\left(\frac{T^{'}}{(dT/dP)_{1000}} - P^{'}\right) \tag{4}$$

where $T^{'}$ is the park phase temperature anomaly defined by $T^{'} = T - \bar{T}$ with $\bar{T}$ being the time average temperature, $P^{'}$ is the park phase float displacement defined by $P^{'} = P - \bar{P}$ with $\bar{P}$ being the time average pressure, $(dT/dP)_{1000}$ is the constant temperature gradient at 1000 dbar, ρ is the local density at 1000 dbar, and g is the gravitational constant. This final equation allows us to estimate vertical velocity solely using data from Argo floats, with $T^{'}$ and $P^{'}$ calculated from the float trajectory data and with $(dT/dP)_{1000}$ and ρ calculated from the float profile data.

3 Estimation of Argo-float based vertical velocity

3.1 Global Argo Data

Data used in this work include the drift trajectory, profile, technical (e.g. float systems reports during cycles), and metadata (e.g. float cycle configuration information) for the global array of Argo floats. Though there are over 16,000 floats with trajectory information available in the Global Data Acquisition Center (GDAC), many of the cycles from these floats cannot be used in estimating vertical velocity. Data that are usable for these estimates start in August 2005 and continue through April 2022. Data prior to 2005 are not usable because early float versions did not report an adequate number of samples during the drift cycle. Additionally, some later data are not usable because floats deployed by different programs or from different manufacturers report the drift data inconsistently with one another causing the necessary trajectory information to be less-uniformly available compared to that of the profile data. The biggest discrepancy is in the sampling regime during the park cycle, which results in floats reporting data ranging from sparse drift averages up to comprehensive hourly measurements of temperature and pressure. Note that the technical data and metadata for floats are similar to the trajectory data in they are inconsistently implemented between float programs. This can lead to missing file components causing the data from a float to be unusable in estimating vertical velocity. In particular, we are unable to use cycles that report temperature and pressure less frequently than every 6 hours during the park phase as well as cycles that have inadequate geographic coordinates, cycle numbering, and time information. To ensure that our results that are as robust as possible, we have designated several quality control parameters (Section 3.3) in addition to the Argo program quality control system (Wong et al., 2020). In consequence, our vertical velocity estimates are gleaned from 998 floats, encompassing 107,144 estimates.

3.2 Methods

From Eq.4, both the temperature gradient, $(dT/dP)_{1000}$, and the density, ρ, at 1000 dbar are found using float profile measurements. To get representative values for the entire park phase, the profiles directly before and after each individual park phase are averaged. The density at 1000 dbar is computed using the Gibbs-SeaWater Oceanographic Toolbox routines created by McDougall and Barker (2011) and is a function of absolute salinity and temperature at a constant pressure of 1000 dbar. The temperature gradient is determined by finding the least squares best-fit line to the averaged temperature profile within 100 dbar from the parking depth (Hennon et al., 2014) (Figure 1b).

Starting with the raw temperature and pressure data reported during the entire float park, each drift cycle is split into a half-cycle of at least 4 days in length. The tem-

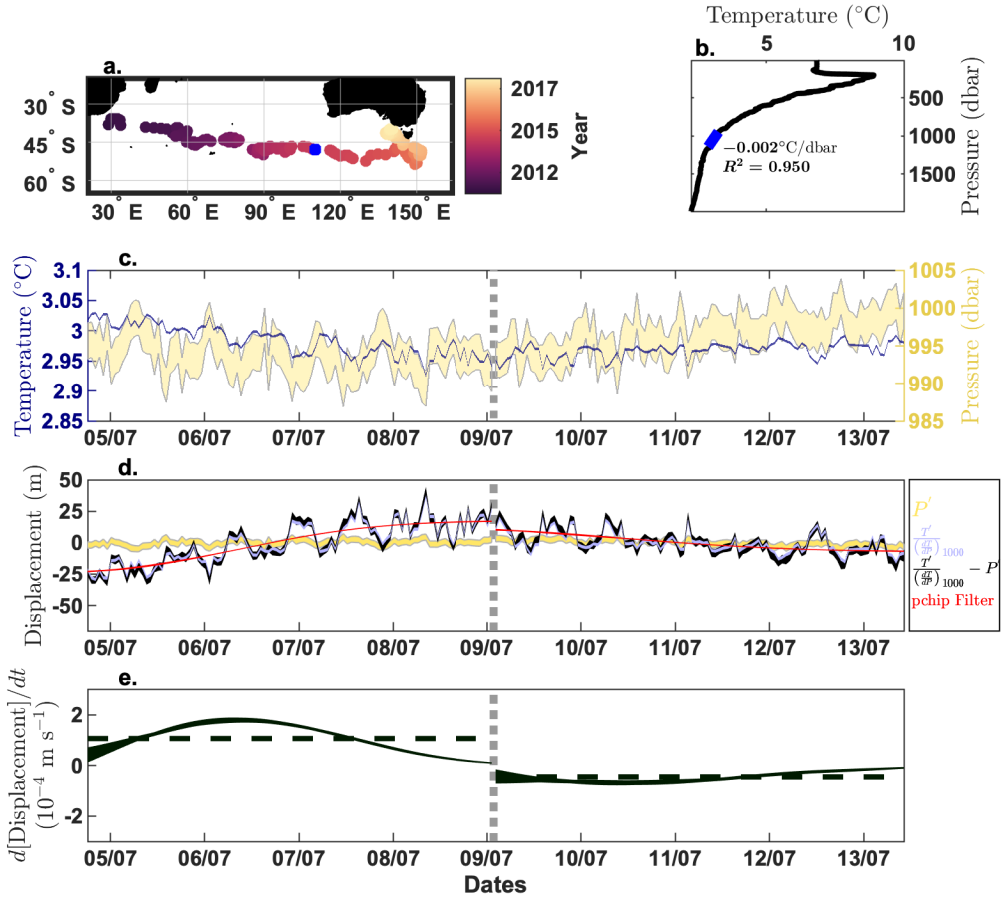

Figure 1. Example process for estimating vertical velocity using cycle number 134 from float 1901150 (WMO ID). No float buoyancy adjustments occurred during this cycle, so we are able to estimate two vertical velocities, one on each side of the gray dashed line in each panel. **a.** Map of all float cycle locations colored by date taken, except cycle number 134 which is noted in blue. **b.** Profile of temperature and pressure from cycle 134 with data surrounding 1000 dbar used to calculate $left(dT/dPright)_{1000}$, with at least 90% linear fit, highlighted in blue. **c.**Hourly sampled trajectory data where the temperature (blue) is shaded as the envelope of 100 iterations of added random error of ±0.002°C and the pressure (yellow) is shaded as the envelope of 100 iterations with added random error of ±2.4dbar, as used in the Monte Carlo simulation described in section 3.3 **d.** Float displacement $P^{'}$ (yellow), isotherm displacement including the float displacement $\frac{T^{'}}{(dT/dP)_{1000}}$ (blue), corrected isotherm displacement $\frac{T^{'}}{(dT/dP)_{1000}} - P^{'}$ (black), and the pchip filter of the corrected isotherm displacement. Note that all of these values are converted to meters using an assumption of hydrostatic balance. **e.** Derivative of the filtered corrected isotherm displacement (solid black) and average value of the derivative (dashed black), which results in vertical velocity estimates of $(7.6 \pm 0.1) \times 10^{-5}$ m s^{-1} and $(-3.0 \pm 0.1) \times 10^{-5}$ m s^{-1} on the left and right sides of the cycle, respectively. Note that the error of these estimates is taken from the standard deviation of the 100 estimates that resulted from the Monte Carlo iterations.

perature and pressure anomalies during the park, $T^{'}$ and $P^{'}$, are found by subtracting the half-cycle mean values from the data for each half-cycle (Figure 1c). These anomalies are then applied to Eq.(4) to find the corrected isotherm displacement (Figure 1d). To examine phenomena on longer than inertial time scales, we use a fourth order low-pass Butterworth filter with a cutoff frequency of 0.3 cycles per day on the corrected isotherm displacement with odd reflected endpoints. This effectively removes high frequency variability caused by internal tides and other short-lived events (Hennon et al., 2014). After filtering, we fit the data using a piecewise cubic Hermite interpolating polynomial (pchip) (Fritsch & Carlson, 1980) and take the derivative with respect to time to get the slopes of the data during the drift half-cycle. We then take the average of this derivative and convert to depth units by assuming hydrostatic balance (as was done to reach Eq. 4) and using the density calculated from the profile, giving us approximate values for the half-cycle-average vertical velocity (Figure 1e).

3.3 Quality Control

After a measurement cycle occurs, floats transmit to the data acquisition centers via the Argos-2 (<1% of usable floats) or the Iridium (>99% of usable floats) satellite systems. Then the data go through an automated quality control process that checks for reasonable dates, locations, velocities, pressures, temperatures, and salinities (Wong et al., 2020; *Argo user's manual*, 2022). Values are flagged with identifiers ranging from 1 to 4, where 1 corresponds to good data and 4 corresponds to bad data. This project uses quality control flags equal to 1, 2, or data that have been adjusted to reach the same level of qualification (Wong et al., 2020). Within 24 hours after a float surfaces, the data have gone through the process described above and are publicly available as *Realtime-mode* data. In the following 5 months, more rigorous quality control should be done updating the cycle label to *Delayed-mode* (Wong et al., 2020). However, this step is often only applied to the profile and not to the trajectory data, the technical data, or the metadata. For estimating vertical velocity, we use the *Delayed-mode* data for the selection of floats where it is available (23.5% of usable cycles) and the *Realtime-mode* data in all other cases.

As stated in section 2, the vertical temperature gradient must be linear to maintain the assumption that there are limited vertical mixing effects on temperature. To enforce this condition, only cycles where the least squares best-fit line accounts for at least 90% of the temperature variance are considered (Hennon et al., 2014). In some cases, the slope estimated from the profile data was near zero resulting in the magnitude of our vertical velocity estimates being unreasonably large. To counteract these cases, any vertical velocity with a magnitude larger than 10 standard deviations away from the mean of all the estimates are neglected (<0.05% of estimates).

Due to differences in float manufacturing and measurement goals, not all floats are programmed in the same manner. In particular, floats do not all have the same parking pressure and do not report data at the same interval during the drift. To keep the vertical velocity estimates comparable to one another, only floats that are assigned a park pressure of 1000 dbar in their metadata have been used. For differing drift data intervals, only floats that report both temperature and pressure measurements at a minimum of 6-hourly time increments during the park phase have been included. Previous studies that have analyzed isotherm displacement during the drift cycle could only use hourly-reporting floats because they were trying to capture the signal from internal gravity waves and tides (Hennon et al., 2014). The mesoscale vertical velocities we are estimating persist over somewhat larger time scales, so we can use floats with a longer time between samples. As confirmation that the 6-hourly floats supply sufficient resolution, we conducted a test where we sub-sampled the hourly floats to every 6 hours, with randomly selected initial points, and re-estimated the vertical velocity using our method. When comparing the initial velocity estimates from the hourly samples with those from the sub-

sampled regime, there is a 91% correspondence in the linear fit; the slope of this linear fit is 0.87. Though the 6-hour sub-sampling does slightly cause our method underestimate the vertical velocity magnitude, particularly at large values, we feel that this the error is sufficiently small with the average difference between the 6-hour sub-sampled values and the hourly true values being 2.2×10^{-7} m s^{-1}. Floats that measure once per day or transmit a cycle average value do not capture the necessary temperature variability to estimate isotherm motion around the float and are therefore discarded.

To maintain the programmed park pressure, floats will internally adjust their buoyancy under certain conditions. If a float is pushed outside of a pre-determined threshold (most often ± 10 dbar, located in the float metadata) from the programmed park pressure for three hours consecutively, the float increases or decreases its buoyancy to move back into the target zone. This adjustment causes additional variability in temperature measurements that is difficult to distinguish from temperature variability caused by isotherm displacement alone. Buoyancy adjustments can happen multiple times in a single drift cycle and the floats then report the number of times that they adjust in their technical data; however, they do not report when the adjustments actually occur. To manually determine when an adjustment happens, hourly data are required. Thus, for floats with a lower sampling frequency than hourly any cycles with reported adjustments are discarded. For floats that do measure on an hourly basis, we use the pressure data to compute the time of adjustment and keep only those cycles where the number of computed adjustments equals that reported in the technical data. Only half-cycles with no adjustments (omitting data in a 6 hour window after any prior adjustments) were used to compute vertical velocity. The floats do adjust preferentially in certain areas, which can likely be attributed to large magnitude vertical motions influencing the floats. Because we are neglecting cycle halves that include these adjustments, the estimates for vertical velocities shown in this paper can be considered conservative.

To estimate the error involved in calculating the vertical velocity, we have conducted a Monte Carlo simulation that incorporates random error based on instrument accuracy. Floats are equipped with CTD sensors that have published accuracy of ±0.002°C (0.0002°C drift per year) and ±2.4 dbar (0.8 dbar drift per year) for temperature and pressure, respectively (Wong et al., 2020). Because the average values are removed during the calculations, the precision of each measurement are a more likely to impact the observation quality, but these values are smaller than those of the accuracy. We feel confident that using the larger values allows for robust testing in the Monte Carlo simulation. For each calculation of vertical velocity, 100 iterations of random error within the accuracy ranges were incorporated into the temperature and pressure data. These data were then used to compute 100 estimates of vertical velocity for each half cycle. The final value is the average of all the different iterations and the error is assumed to be represented by the standard deviation (Figure 1c). To compute aggregate statistics (mean, median, variance, etc.) on subsets of the data, we use all 100 of the Monte Carlo iterations for each half cycle and report the average of the desired statistic along with the standard deviation as our error estimate.

4 Results

4.1 Global estimates of near 1000-meter vertical velocity

The locations of vertical velocity estimates from the global Argo array have a spatial distribution that varies widely across geographic regions (Figure 2 a-c). Though the Argo array is well-distributed globally (Wong et al., 2020), these estimates of vertical velocity do not have uniform coverage and are particularly sparse in the Atlantic and North Pacific Oceans (Figure 2c). This is due to a lack of adequate 1000 dbar drift data in those areas in addition to a rigorous application of quality control measures (section 3.3).

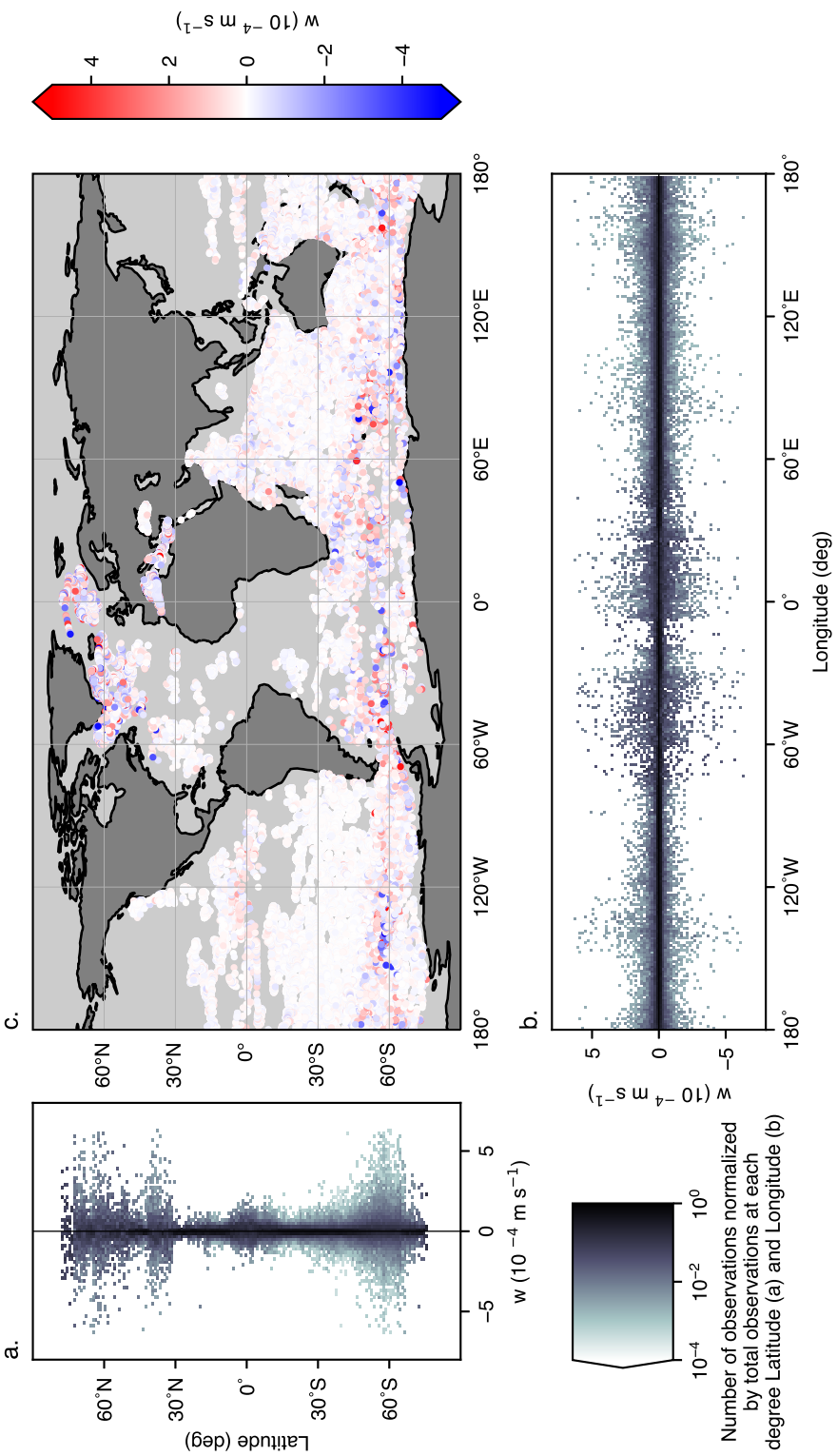

Figure 2. Argo-based, 5-day-averaged vertical velocities near 1000 dbar. Probability density functions of velocities as a function of (a) latitude and (b) longitude, normalized at each degree latitude or longitude, respectively. (c) Global map of all individual velocity estimates.

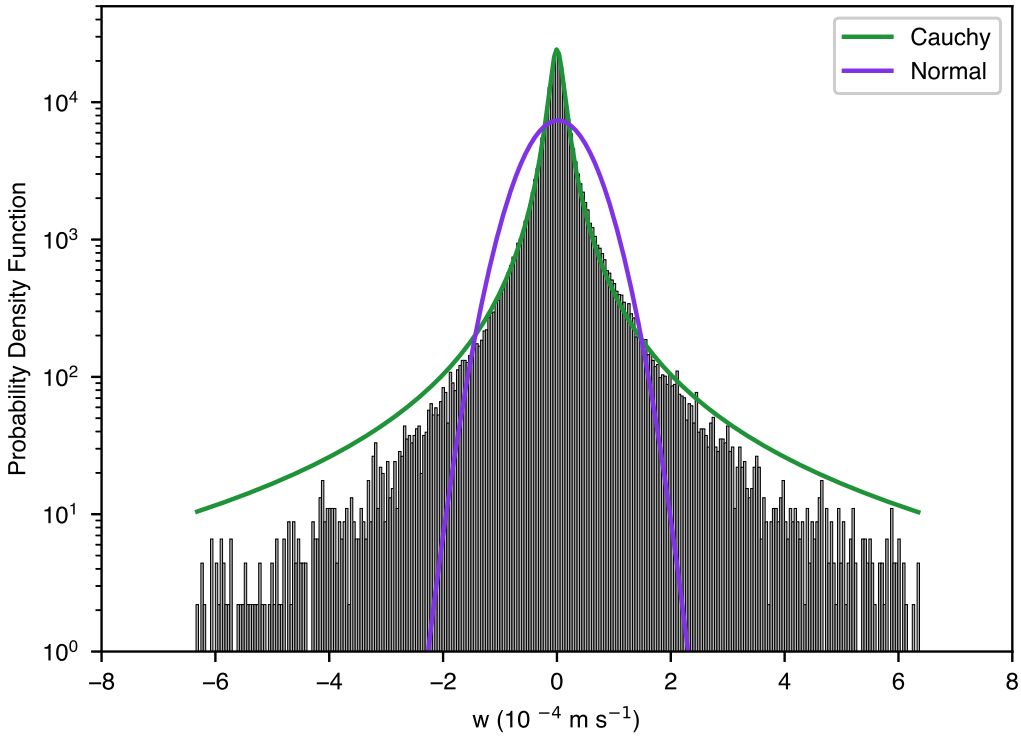

Figure 3. Probability density function (PDF) of global vertical velocities with Cauchy (green) and Normal (purple) distributions plotted atop. Note that the y-axis is on a logarithmic scale.

The estimated vertical velocities have a particularly heavy-tailed distribution with a high peak (Figure 3). These data have the smallest sum square error (defined as $\sum_i (y_i - f(x_i))^2$, where y_i is the given histogram value and $f(x_i)$ is the value predicted by the probability density function) when fit by the Cauchy function as Eq. 5,

$$f(x) = \frac{1}{\pi(1 + x^2)} \tag{5}$$

which is the equivalent to a Student's t continuous fit with one degree of freedom (Forbes et al., 2010). In comparison, a normal distribution is equivalent to a Student's t continuous fit with infinite degrees of freedom, meaning that these data are decidedly non-Gaussian (Forbes et al., 2010). One characteristic of a Cauchy probability distribution is that the higher order statistical moments are undefined and do not converge with increased sampling (Forbes et al., 2010; Sugiyama, 2016). Therefore, the mean and standard deviation that we compute for our finite dataset are highly dependent on the selection of sampling parameters and do not converge for large sample size. To characterize our dataset, we compute and report the median, which is less influenced by heavy tails. We also examine the mean and standard deviation for our data with the caveat that these values are dependent on the particular characteristics of sampling. With this in mind, this type of statistical analysis can still help provide insight into the variability of our estimates.

The median vertical velocity from the entirety of our estimates, is $(1.3 \pm 0.2) \times 10^{-7}$ m s^{-1} and the average vertical velocity is $(1.9 \pm 0.02) \times 10^{-6}$ m s^{-1}. If these data were collected everywhere globally, over a sufficiently long time period, the true average would be equivalent to zero due to the conservation of mass in the ocean (Stommel & Arons, 1959; Freeland, 2013). However, there is no evidence to suggest that the ver-

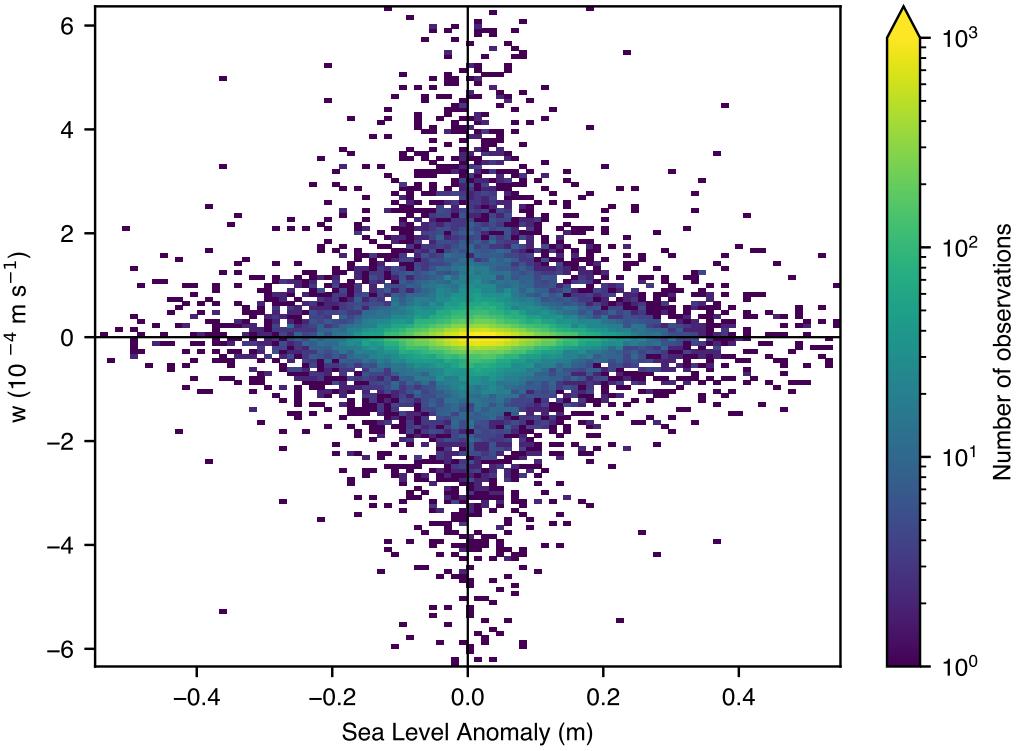

Figure 4. Global Sea Level Anomaly (SLA) vs. Vertical velocity estimates colored by the number of observations for each 0.01m $\times 10^{-5}$m s^{-}1 box

tical motion occurring at just the mesoscale should be balanced within itself, so we cannot assume that the average of our irregularly-sampled, mesoscale estimates should be equal to zero. The variance of our vertical velocity estimates is $(3.0 \pm 0.01) \times 10^{-9}$ m s^{-1}, which is impacted by both the high peak and heavy-tails of our distribution. There is a slight positive skew of 0.6±0.03; however, due to the shape of the distribution discussed above, we cannot disentangle if this is a product of the uneven spatial and temporal distribution of our samples or a product of actual physical phenomena. To gain different insights into these estimates, we examine areas that are well sampled in context with sea level anomaly.

4.2 Sea level anomaly

To examine how our mid-depth vertical velocity estimates correspond with other physical phenomena in the ocean, we use the Data Unification and Altimeter Combination System (DUACS) gridded (L4) altimeter product with a 1/4° × 1/4 ° resolution with daily data ranging from 1993 to June 2020 (CMEMS, 2021). From this gridded product, we use both the Sea Level Anomaly (SLA) and the horizontal (zonal [U] and meridional [V]) absolute geostrophic velocities at the surface.

The SLA in this dataset is given as the sea surface height above mean sea surface using a 20 year mean from 1993 through 2012; however, to better compare this data with that given by the Argo array, we have changed the reference period to be a 15 year mean from 2005 through 2020 following the methods in Pujol et al. (2016). To directly link float estimates with satellite SLA, we located the nearest grid cell in the DUACS L4 product to each vertical velocity estimate location and averaged the SLA at that point for

the actual dates of the float cycle. We repeat the process for the horizontal velocity magnitude, computed from surface U and V, by finding the nearest grid cells in the satellite product to our float estimates. However, we then average across all times(1993-2012) rather than just the float period. Taking the average over the entire time-series results in a mean state horizontal velocity, to which we can compare our vertical velocity.

Investigating the SLA from all locations where we have half cycles, we see that there is no distinct correlation between the SLA and the vertical velocity estimates (Figure 4). The highest values of vertical velocity would visually appear to be associated with smaller magnitude SLA, but there are a considerably more data points present at smaller magnitudes than at higher magnitudes for both the vertical velocity and SLA (note Figure 4 has an exponential colorbar). Statistically this pattern is simply a product of the high peaks in both the vertical velocity and SLA distributions rather than showing a particular physical phenomena. Additionally, the SLA is measured at the surface via satellites, so comparing these measurements to our mid-depth estimates of vertical velocity is not direct. Certainly, not every eddy has a subsurface component that will have an effect at the Argo parking depth. There are ways to locate sub-surface phenomena solely using satellite data (Assassi et al., 2016); however, these methods have difficulty in complex areas with strong currents, of which a great deal of our study area is composed. Instead, separating our vertical velocity estimates and their associated SLA into subsets of areas with high coverage will allow us to examine the degree of variability between different locations.

4.3 Spatial variability and areas of interest

Because of the varying data density across the globe, spatial analysis of the entire data set is not wholly informative. We have selected a few key areas for comparison. Namely, we chose two major topographic features in the Antarctic Circumpolar Current (ACC) in the Southern Ocean (Kerguelen Plateau (KP) and Pacific-Antarctic Ridge (PAR), Figure 5 d-e) and selected juxtaposed examples in the gyres north of each (Indian Ocean Gyre (IOG) and Pacific Ocean Gyre (POG), Figure 5 b-c). Each of these subsets of data has a comparable number of observations rather than equal study areas. We find that the distributions of vertical velocity estimates over topographic features are similar to the global distribution in that they have high peaks and heavy tails that are best fit by the Cauchy function (Figure 5d-e). Our estimates in quiescent areas have much lighter tails and, though still not entirely normally distributed, are better fit by a normal distribution across most of the estimates with the only misfits being infrequent, high-magnitude events appearing in the tails (Figure 5 b-c).

The median, mean, and variance of our vertical velocity estimates for each of the selected areas from Figure 5 are shown in Table 1. The mean values are similar in magnitude for the more energetic areas (KP, PAR) on the order of 10^{-6} to 10^{-5} m s^{-1}, as well as for the more quiescent areas (IOG,PAR) on the order of 10^{-7} m s^{-1}. However, due to the heavy-tailed distributions, all of the mean values depend on the particular sampling scheme selected, even for large sample sizes, so these average results must be interpreted with caution. The differences in variance are more illuminating. In the ocean gyres, the variance of our estimates are on the order of 10^{-10} [m s^{-1}]^2 while the topographic features have a variance nearer to 10^{-8} and 10^{-9} [m s^{-1}]^2 for PAR and KP, respectively. This emphasizes the impact that the high-magnitude, heavy tails have in areas with significant bathymetry. As another large topographic feature in the ACC, we expect to see a similar pattern for Drake Passage (DP) (Figure 5g). Though the estimates in this area are sparser than in the others, the variance is once again two orders of magnitude larger than those of the ocean gyres and comparable to the other active regions. The scale of the global variance is approximately 10^{-9} [m s^{-1}]^2, showing the impact of the large vertical velocities that are localized in space.

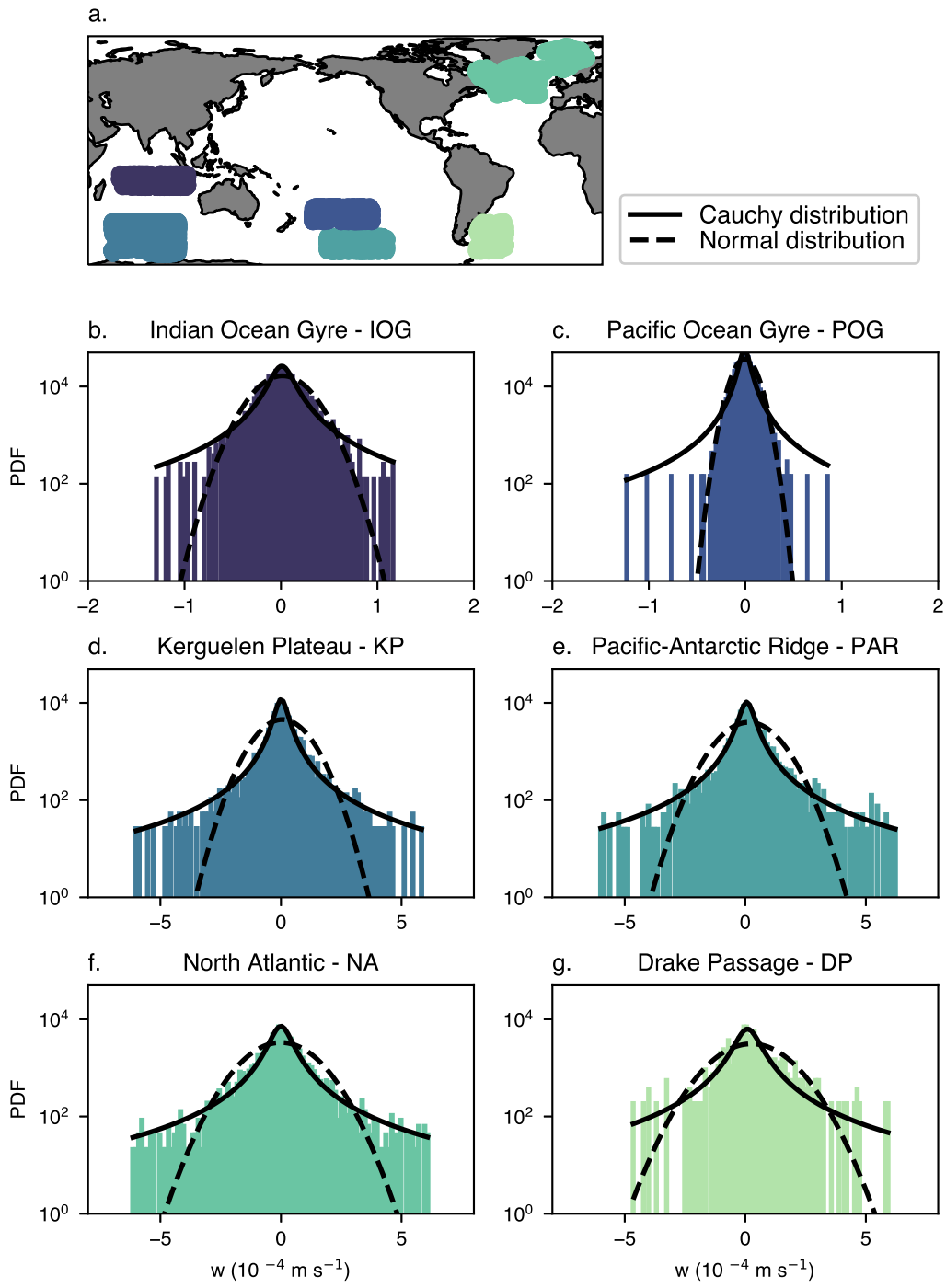

Figure 5. Probability density function distributions with Normal and Cauchy distribution functions plotted on top for select areas highlighted by corresponding color in a global map (a). b) Indian Ocean Gyre [IOG] with 3,001 observations, c) Pacific Ocean Gyre [POG] with 3,143 observations, d) Kerguelen Plateau [KP] with 3,057 observations, e) Pacific-Antarctic Ridge [PAR] with 3,053 observations, f) North Atlantic [NA] with 3,664 observations, g) Drake Passage [DP] with 487 observations. Note that the x axes on panels (b) and (c) are decreased by a factor of 4 from the other PDFs.

Table 1. Aggregate statistics (mean, median, variance) of vertical velocity estimates globally and for selected areas shown in Figure 5.

Area	Median (m s^{-1})	Mean (m s^{-1})	Variance ([m s^{-1}]^2)
Global	$(1.3 \pm 0.2) \times 10^{-7}$	$(1.9 \pm 0.02) \times 10^{-6}$	$(3.0 \pm 0.01) \times 10^{-9}$
KP	$(1.2 \pm 0.2) \times 10^{-6}$	$(5.4 \pm 0.2) \times 10^{-6}$	$(7.8 \pm 0.09) \times 10^{-9}$
IOG	$(7.3 \pm 1.4) \times 10^{-7}$	$(8.5 \pm 0.7) \times 10^{-7}$	$(4.5 \pm 0.05) \times 10^{-10}$
PAR	$(7.4 \pm 0.2) \times 10^{-6}$	$(1.4 \pm 0.02) \times 10^{-5}$	$(1.0 \pm 0.01) \times 10^{-8}$
POG	$(-6.2 \pm 0.9) \times 10^{-7}$	$(-4.7 \pm 0.4) \times 10^{-7}$	$(1.2 \pm 0.01) \times 10^{-10}$
DP	$(1.1 \pm 0.1) \times 10^{-5}$	$(2.5 \pm 0.07) \times 10^{-5}$	$(1.7 \pm 0.03) \times 10^{-8}$
NA	$(-1.2 \pm 0.3) \times 10^{-6}$	$(-6.1 \pm 2.3) \times 10^{-7}$	$(1.5 \pm 0.01) \times 10^{-8}$

Another area of interest is the North Atlantic (NA, Figure 5f), where the vertical velocity distribution is similar to the high energy areas of the Southern Ocean. As a region with mixed layers exceeding 1000 m, deep water formation, and significant eddy activity (Stommel & Arons, 1959; Ferrari & Wunsch, 2009), it is expected that the North Atlantic mimics the other active regions. Indeed, the variance is once again two orders of magnitude larger than that of the quiescent areas.

The median values of our vertical velocity estimates range from 10^{-7} to10^{-5} m s^{-1} (Table 1). The larger values occur in high energy areas while the smaller values occur in the gyres. The global median is on the same order of magnitude as the gyre median values. This shows that, though the effects of large-magnitude events can be seen in the global variance, the small-magnitude phenomena that form the high peak in the distribution dominate the median (and mean).

The SLA associated with our select areas also highlight the variability between different locations. The SLA in the IOG and POG (Figure 6ab) are similar in range going from -0.33 to 0.35 m with small vertical velocities. However, the SLA in the PAR (Figure 6d) is more limited only ranging between -0.11 to 0.15 m with larger vertical velocities. Even more different are the SLAs near the KP (Figure 6c), where the range of both SLA (-0.49 to 0.41m) and vertical velocity are wide. This reinforces that there is high variability in the spatial distribution of vertical velocities that are interacting with a variety of mechanisms, even in similarly energetic regimes.

4.4 Southern Ocean bathymetry

To examine additional factors that may impact the observed vertical velocity variability, we utilize the ETOPO1 1 Arc Minute Global Relief Model (Amante & Eakins, 2009; NGDC, 2009). We use the version of this dataset that includes bathymetry at the base of the Antarctic and Greenland ice sheets. To better compare between the gridded relief model and the Argo array, we located the nearest grid cell to each float cycle location that contains an ocean depth. Because bathymetry changes on time scales much longer than the mesoscale phenomena we are focused on, we assume that the bathymetry remains constant.

By selecting both bathymetric and vertical velocity data from a large region with dense coverage, we can observe the changes in vertical velocity magnitude variability as it is related to space. Analyzing only estimates in the Southern Hemisphere, where the

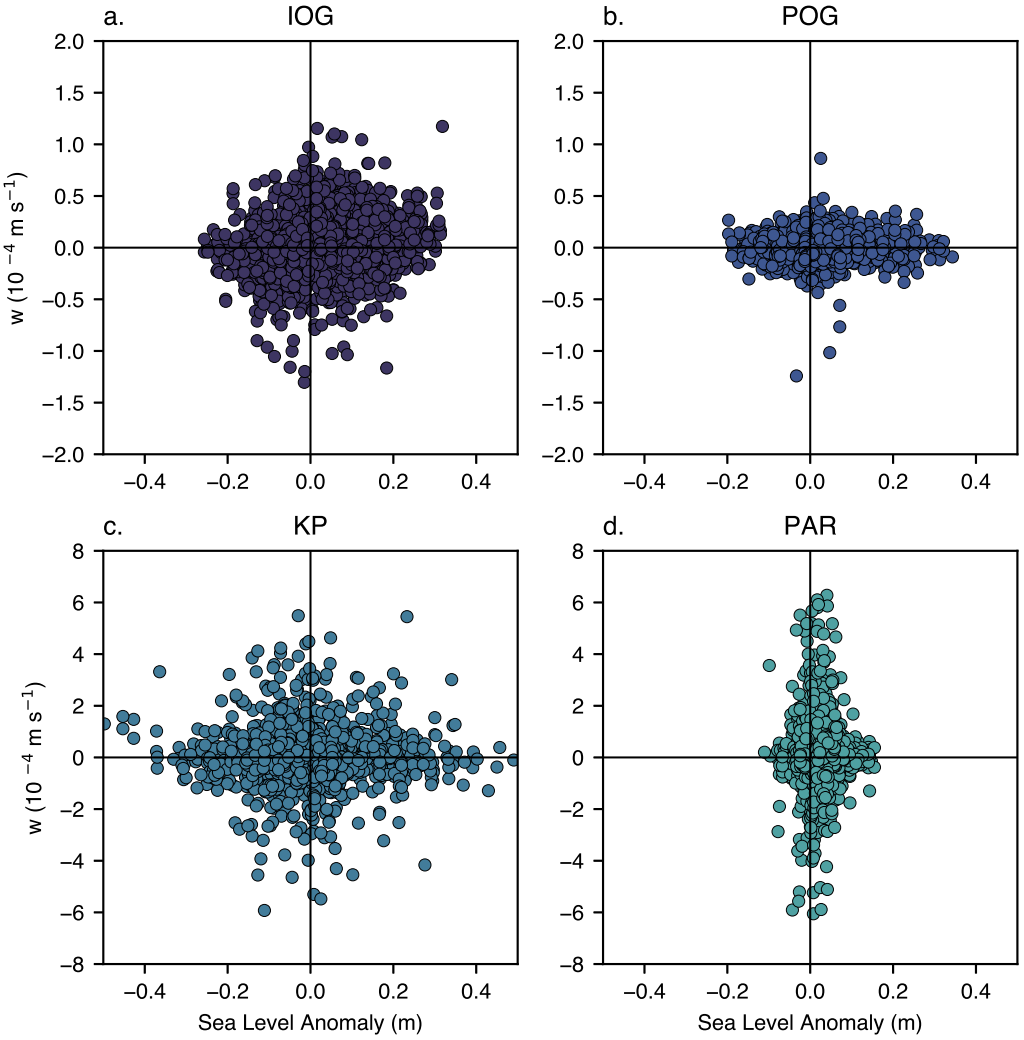

Figure 6. DUACS Sea Level Anomaly at the nearest grid point averaged over time of corresponding half cycles (as described in section 4.2 versus vertical velocity estimates for select areas highlighted by corresponding color in a global map in Figure 5a. a) IOG, b) POG, c) KP, d) PAR. Note that the y axes on panels (a) and (b) are decreased by a factor of 4 from panels (c) and (d).

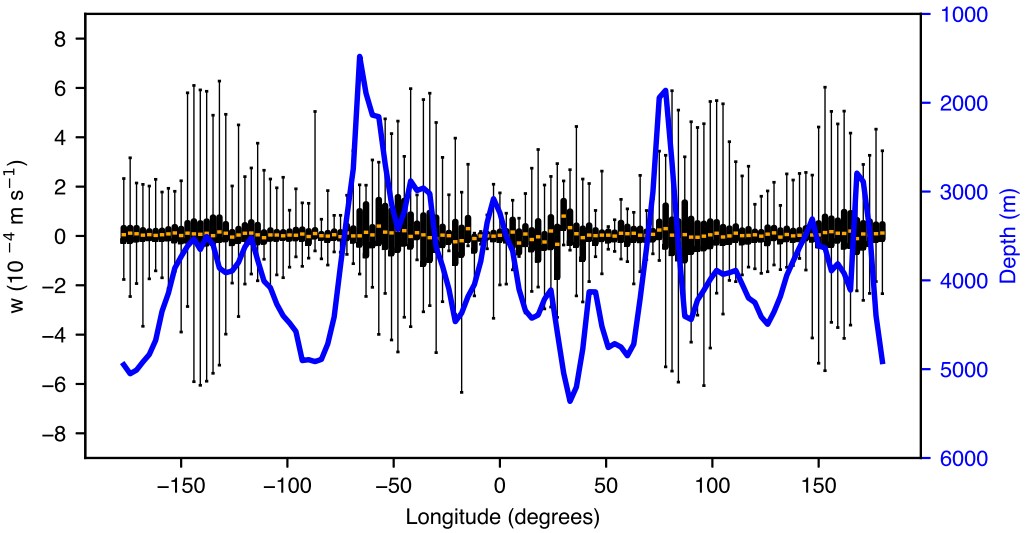

Figure 7. Southern Ocean bathymetry from ETOPO1 averaged meridionally between 50°S and 60°S (blue) plotted on top of box plots showing the distributions of vertical velocity estimates in 3° longitude sections between 50°S and 60°S, where the orange line corresponds to the median value, the box corresponds to the 25th and 75th percentiles, and the error bars correspond to full range of vertical velocity magnitudes in each area.

majority of our data reside, we find that there are a larger number of high-magnitude values between -60°N and -40°N (Figure 2a), as well as ample low-magnitude estimates in this region. The distribution is similar to the full data set with its particularly heavy tails coupled with a high peak. This latitude band corresponds with the general area of the ACC, which generates a considerable number of mesoscale and sub-mesoscale phenomena where we would expect higher magnitude vertical velocities (Rosso et al., 2014; Cusack et al., 2017). Looking closer at the variation in longitude (Figure 2b), we can see that the higher magnitude velocities do not occur uniformly, but instead have a unique distribution with certain areas being hot spots of higher magnitude vertical velocity.

Consistent with the results discussed in section 4.3, these hot spots correspond roughly to known bathymetric features in the path of the ACC, including KP, PAR, DP from Section 4.3 as well as Macquerie Ridge (Tamsitt et al., 2017).To quantify the relationship between bathymetry and vertical velocity, we compute the lagged correlation between ocean bottom depth from ETOPO1 and absolute vertical velocity, both of which are first averaged in geographic bins that span 50°S to 60°S in latitude and 3° in longitude.The correlation between average vertical velocity and bathymetry peaks ($r = 0.438$) when w lags the average bottom depth by 12° longitude. This highlights that, in general, higher magnitude values occur downstream of elevated topography. Averaging instead across all latitudes of the Southern Hemisphere gives a maximum correlation between absolute vertical velocity and bottom depth of 0.267, smaller than the correlation found for the ACC alone. This implies that bottom topography has a bigger impact on vertical velocity variability in the Southern Ocean than it does in the global ocean as a whole.

An additional factor that may impact the distribution of 1000-m vertical velocities is the strength of the horizontal flow. Examining the global surface velocities from satellites (as described in section 4.2) with their corresponding float w estimates, we see

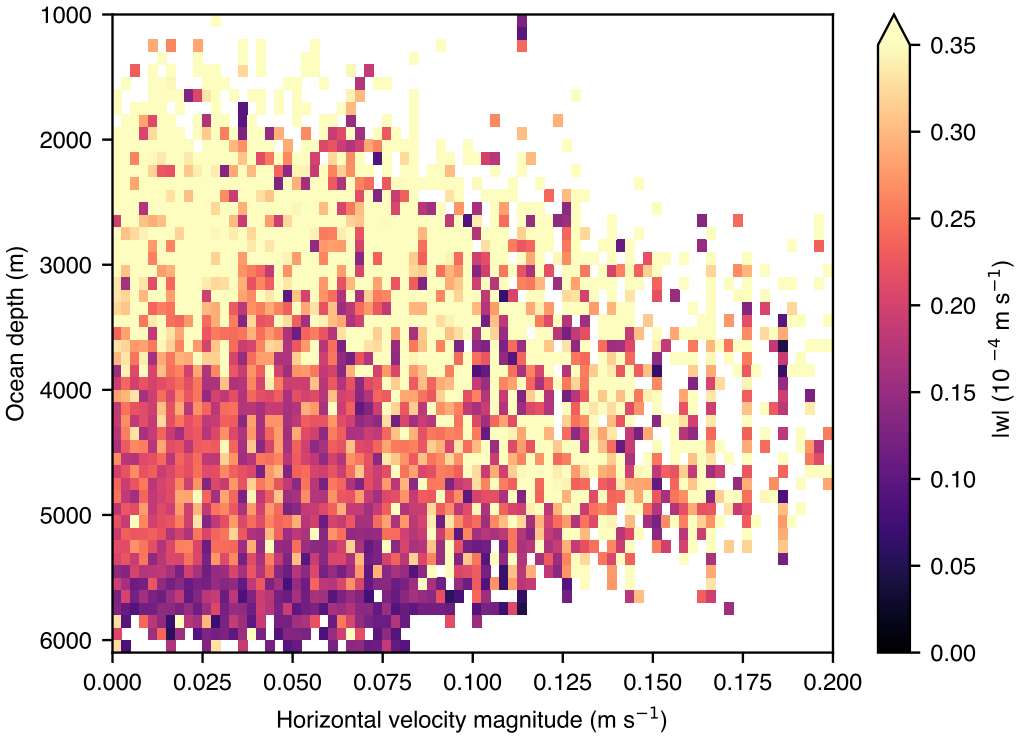

Figure 8. Average absolute value vertical velocity within grid cells of horizontal surface velocity averaged over 1993-2020 (bin size of 0.0025 m s^{-1}) and ocean depth (bin size of 75 m). Only grid cells with at least 5 estimates of vertical velocity are shown here. Note that floats are typically not deployed in waters shallower than 2000 m (due to a desire to prevent float grounding) so sparseness in samples above this depth is expected.

that deep areas with small horizontal surface velocities tend to have smaller values of w. However, areas with larger average horizontal surface flow ($> 0.08\text{m s}^{-1}$) have more high magnitude vertical velocities, even where the ocean is deep (between 4000-5000 m) (Figure 8).

Taken altogether, these results indicate that at mid-depths, higher vertical velocities occur downstream of shallow bathymetry and in areas with increased horizontal velocities at the surface (Figure 8), such as the ACC. Prior research has shown elevated mesoscale eddy activity frequently occurs where strong horizontal flows cross over topographic features (Rosso et al., 2014; Cusack et al., 2017; Liang et al., 2017). These findings align very well with the results presented here, providing evidence that the 5-day average vertical velocities determined from Argo observations primarily reflect mesoscale phenomena.

5 Discussion and conclusions

The results presented here are the first estimates of subsurface vertical velocity determined directly from observations, across wide swaths of the global ocean. Our approach of using measurements from floats in the globally distributed Argo array provides insight into three-dimensional flows occurring near 1000 dbar. The sampling distribution is uneven, with some regions well covered and others lacking data entirely, due to differences in how floats report data from the drift phase at the parking depth. As the global Argo array continues to evolve, drift data suited for this method will continue to be collected from many floats, thereby increasing the coverage of these vertical velocity estimates (Riser et al., 2016; Roemmich et al., 2019; Wong et al., 2020; *Argo user's manual*, 2022). Furthermore, we encourage all float manufacturers and users to measure and report hourly temperature and pressure data during the drift phase when possible, to expand the spatial coverage of these vertical velocity estimates.

In areas with adequate sampling, our results highlight distinctive spatial variability in vertical velocities at 1000 dbar. In particular, there is clear evidence of a relationship between vertical motion and topographic features, with further influence in areas with strong horizontal flows. This topographic dominance is consistent with prior global estimates of mid-depth vertical velocity using model fields (Liang et al., 2017). To better assess our estimates in relation to velocity output from a widely-used ocean state estimate, we retrieved data from the latest Estimating the Circulation and Climate of the Ocean (ECCO) project (version 4, release 4) (Forget et al., 2015). We used the monthly-averaged vertical component of velocity from 2004 to 2017, which best overlaps with the time period available for the float estimates. We took the $1/2^\circ$ resolution LLC90 grid, chose the depth level closest to 1000 dbar, and then selected only locations that have at least one float estimate of vertical velocity within 50km of center of the model grid-cell. Subsampling the model output in this way eliminates data from the coastal areas and shallow areas where floats do not sample.

Averaging the resulting model vertical velocity fields over the full 13-year period reveals spatial variability that matches the spatial pattern in the Argo-based estimates remarkably well. This similarity again emphasizes the topographic influence on vertical motions near 1000 dbar (Figure 2, Figure 9). The ECCO vertical velocities in Figure 9 are an order of magnitude smaller than the float-based velocities in Figure 2, reflecting the difference in the temporal scales of the two estimates.

Examining instead the monthly-averaged velocities from ECCOv4.4, again restricted to only the locations of the float estimates, the normalized distribution of vertical velocity exhibits a high peak and heavy tails that is best fit by the Cauchy distribution, like the float-based estimates.

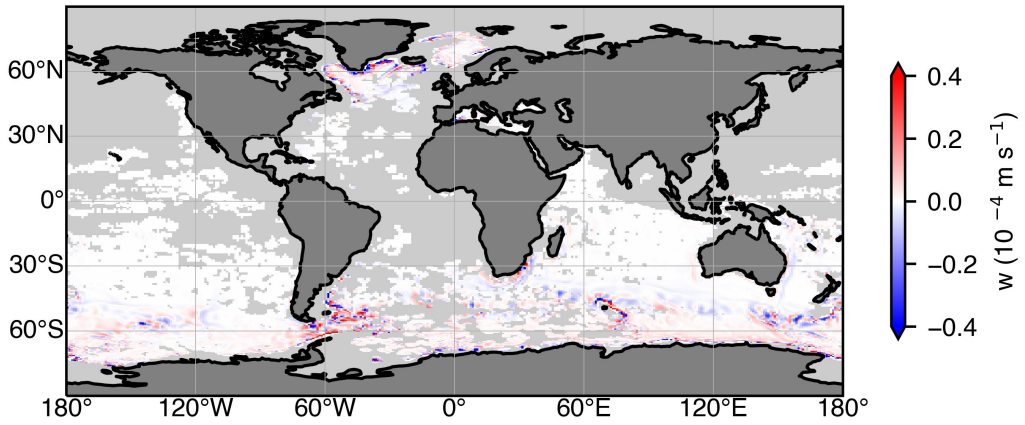

Figure 9. Global map of the vertical velocity field from the ECCOv4.4 model in grid cells that contain observational estimates from floats.

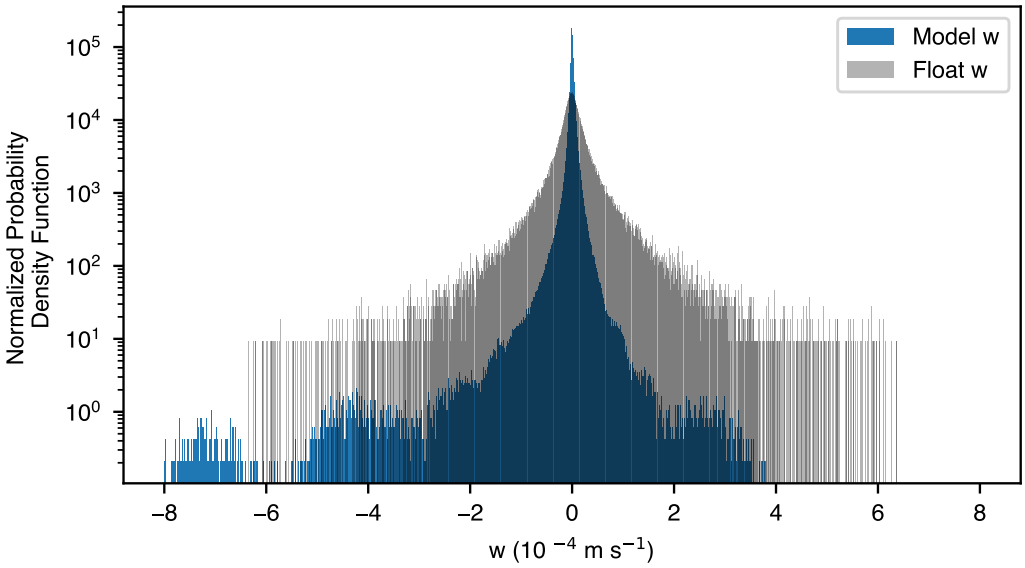

Figure 10. Distributions of model vertical velocity (blue) and observational estimates (gray), with each bin showing the count in the bin divided by the total number of observations and by the bin size (1×10^{-6} m s^{-1}).

Although the 5-day averaged float estimates and the monthly model w fields still have different temporal scales, the similarity in the shape of the distributions provides support for the efficacy of the vertical velocity estimation method described here. Interestingly, the distribution of the observational w estimates is more symmetric than the distribution of the model vertical velocities, which is skewed towards negative values. Possible reasons for this include the uneven temporal spacing in the float estimates when compared to the model field, potential spatial sampling biases in the float estimates, or inadequate representation of mesoscale motions in the model. In addition, the tails of the float-based distribution decrease monotonically, while the model-based distribution exhibits multiple local maxima in both tails, likely due to limitations of the model's vertical resolution (Wong et al., 2020; Forget et al., 2015; Liang et al., 2017).

Advecting a synthetic float using model velocity fields and then recreating our vertical velocity estimation procedure might appear to be an ideal way to validate this technique.Unfortunately, the spatial and temporal scales required to accurately represent all the relevant dynamics, from the float interactions with the surrounding waters to oceanic mesoscale features, are immensely challenging to achieve (Swift & Riser, 1994; Liang et al., 2017; Wang et al., 2020).Thus a direct model-based validation of the method developed here remains outside of the scope of this work.

The direct estimates of 1000-dbar vertical velocity given here would not be possible without high-frequency data from the parking phase of Argo profiling floats. Though measuring vertical velocities was not an original intention of the Argo program (Riser et al., 2016; Roemmich et al., 2019), being able to adapt this globally-distributed in situ observational data set for novel methods such as the one presented here has immensely increased its scientific value. Continued improvements in float technology will allow for refinement and expansion of this method, as well as the development of others. These capabilities are made possible by the dedicated efforts of the international Argo program to ensure that all float data (i.e. trajectory, technical, metadata, and profile data) are provided in a consistent, quality-controlled format.

The estimates of w computed here directly from Argo float drift observations fit well within the range of values given by prior studies (Stommel & Arons, 1959; Liang et al., 2017; Martin & Richards, 2001; Pilo et al., 2018; Freeland, 2013; Cusack et al., 2017). The distribution of these velocities, characterized by a narrow peak and heavy tails, emphasizes the distinctly non-Gaussian nature of vertical flows in the interior ocean. The variability in 5-day average w at 1000 dbar revealed here provides widespread direct observation-based evidence of the importance of topographic interactions in generating strong vertical motions at the oceanic mesoscale. This novel application of the Argo data set greatly expands our knowledge of the subsurface circulation of the global ocean and provides a unique observational constraint for model validation.

6 Open Research

Float data were collected and made freely available (`https://www.seanoe.org/data/00311/42182/`) by the International Argo Program and the national programs that contribute to it. (`https://argo.ucsd.edu`, `https://www.ocean-ops.org`) (Argo, 2000; Wong et al., 2020). The Argo Program is part of the Global Ocean Observing System.

Bathymetry data from the ETOPO1 1 Arc Minute Global Relief Model are openly available via `https://doi.org/10.25921/fd45-gt74` (Amante & Eakins, 2009; NGDC, 2009). Sea level anomaly and surface horizontal velocities were obtained from the DUACS L4 gridded altimeter product and are available via `https://doi.org/10.48670/moi-00148` (CMEMS, 2021). Model data from the ECCO project (v4r4) are available from the ECCO data server via `https://ecco.jpl.nasa.gov/drive/files/Version4/Release4/` (Forget et al., 2015; Fukumori et al., 2019).

Acknowledgments

This work was supported by National Aeronautics and Space Administration award 80NSSC19K1252 and by National Science Foundation grants OPP-1936222, OCE-1946578, and OCE-2110258. Additionally, we gratefully acknowledge the generous continuing support of the U.S. Argo program by the National Oceanographic and Atmospheric Administration through grant NA20OAR4320271.

References

Amante, C., & Eakins, B. W. (2009). Etopo1 arc-minute global relief model: procedures, data sources and analysis. *NOAA Technical Memorandum NESDIS NGDC-24*.

Argo. (2000). *Argo float data and metadata from global data assembly centre (argo gdac)* [dataset]. SEANOE. Retrieved from `https://doi.org/10.17882/42182` doi: 10.17882/42182

Argo user's manual (Report (Normative document (norm, referencial, protocol))). (2022). doi: https://doi.org/10.13155/29825

Assassi, C., Morel, Y., Vandermeirsch, F., Chaigneau, A., Pegliasco, C., Morrow, R., ... Cambra, R. (2016). An index to distinguish surface- and subsurface-intensified vortices from surface observations. *Journal of Physical Oceanography*, *46*(8), 2529 - 2552. Retrieved from `https://journals.ametsoc.org/view/journals/phoc/46/8/jpo-d-15-0122.1.xml` doi: 10.1175/JPO-D-15-0122.1

CMEMS. (2021). *Global Ocean Gridded L4 Sea Surface Heights and Derived Variables Reprocessed (1993-ongoing) [Data set]* [dataset]. `https://doi.org/10.48670/moi-00148`. (Accessed Oct. 8, 2021) doi: 10.48670/MOI-00148

Cusack, J. M., Naveira Garabato, A. C., Smeed, D. A., & Girton, J. B. (2017). Observation of a large Lee wave in the Drake Passage. *Journal of Physical Oceanography*, *47*(4), 793–810. doi: 10.1175/JPO-D-16-0153.1

Ferrari, R., & Wunsch, C. (2009). Ocean circulation kinetic energy: Reservoirs, sources, and sinks. *Annual Review of Fluid Mechanics*, *41*, 253–282. doi: 10.1146/annurev.fluid.40.111406.102139

Forbes, C., Evans, M., Hastings, N., & Peacock, B. (2010). Cauchy distribution. In *Statistical distributions* (p. 66-68). John Wiley & Sons, Ltd. Retrieved from `https://onlinelibrary.wiley.com/doi/abs/10.1002/9780470627242.ch10` doi: https://doi.org/10.1002/9780470627242.ch10

Forget, G., Ferreira, D., & Liang, X. (2015, oct). On the observability of turbulent transport rates by Argo: Supporting evidence from an inversion experiment. *Ocean Science*, *11*(5), 839–853. doi: 10.5194/os-11-839-2015

Frajka-Williams, E., Eriksen, C. C., Rhines, P. B., & Harcourt, R. R. (2011). Determining vertical water velocities from Seaglider. *Journal of Atmospheric and Oceanic Technology*, *28*(12), 1641–1656. doi: 10.1175/2011JTECHO830.1

Freeland, H. J. (2013, jan). Vertical velocity estimates in the North Pacific using Argo floats. *Deep-Sea Research Part II: Topical Studies in Oceanography*, *85*, 75–80. doi: 10.1016/j.dsr2.2012.07.019

Fritsch, F. N., & Carlson, R. E. (1980). Monotone piecewise cubic interpolation. *SIAM Journal on Numerical Analysis*, *17*(2), 238–246.

Fukumori, I., Wang, O., Fenty, I., Forget, G., Heimbach, P., & Ponte., R. M. (2019). *Ecco version 4 release 4* [dataset]. Retrieved from `https://ecco.jpl.nasa.gov/drive/files/Version4/Release4/doc/v4r4_synopsis.pdf` (Accessed Feb. 27, 2022)

Hennon, T. D., Riser, S. C., & Alford, M. H. (2014, sep). Observations of Internal Gravity Waves by Argo Floats. *Journal of Physical Oceanography*, *44*(9), 2370–2386. doi: 10.1175/jpo-d-13-0222.1

Liang, X., Spall, M., & Wunsch, C. (2017, oct). Global Ocean Vertical Velocity From a Dynamically Consistent Ocean State Estimate. *Journal of Geophysical Research: Oceans*, *122*(10), 8208–8224. doi: 10.1002/2017JC012985

Martin, A. P., & Richards, K. J. (2001). Mechanisms for vertical nutrient transport within a North Atlantic mesoscale eddy. *Deep-Sea Research Part II: Topical Studies in Oceanography*, *48*(4-5), 757–773. doi: 10.1016/S0967-0645(00)00096-5

McDougall, T., & Barker, P. (2011). Getting started with TEOS-10 and the Gibbs Seawater (GSW) Oceanographic Toolbox. *Scor/Iapso Wg127*, 28pp.

Merckelbach, L., Smeed, D., & Griffiths, G. (2010). Vertical water velocities from underwater gliders. *Journal of Atmospheric and Oceanic Technology*, *27*(3), 547–563. doi: 10.1175/2009JTECHO710.1

Munk, W. H. (1966). Abyssal recipes. *Deep-Sea Research and Oceanographic Abstracts*, *13*(4), 707–730. doi: 10.1016/0011-7471(66)90602-4

NGDC. (2009). *ETOPO1 1 Arc-Minute Global Relief Model* [dataset]. NOAA National Centers for Environmental Information. (Accessed Feb. 27, 2022) doi: 10.25921/fd45-gt74

Pilo, G. S., Oke, P. R., Coleman, R., Rykova, T., & Ridgway, K. (2018). Patterns of Vertical Velocity Induced by Eddy Distortion in an Ocean Model. *Journal of Geophysical Research: Oceans*, *123*(3), 2274–2292. doi: 10.1002/2017JC013298

Pujol, M.-I., Faugère, Y., Taburet, G., Dupuy, S., Pelloquin, C., Ablain, M., & Picot, N. (2016). Duacs dt2014: the new multi-mission altimeter data set reprocessed over 20 years. *Ocean Science*, *12*(5), 1067–1090.

Riser, S. C., Freeland, H. J., Roemmich, D., Wijffels, S., Troisi, A., Belbéoch, M., ... Jayne, S. R. (2016). Fifteen years of ocean observations with the global Argo array. *Nature Climate Change*, *6*(2), 145–153. doi: 10.1038/nclimate2872

Roemmich, D., Alford, M. H., Claustre, H., Johnson, K. S., King, B., Moum, J., ... Yasuda, I. (2019). On the future of Argo: A global, full-depth, multi-disciplinary array. *Frontiers in Marine Science*, *6*(JUL), 1–28. doi: 10.3389/fmars.2019.00439

Rosso, I., Hogg, A. M., Strutton, P. G., Kiss, A. E., Matear, R., Klocker, A., & van Sebille, E. (2014). Vertical transport in the ocean due to sub-mesoscale structures: Impacts in the kerguelen region. *Ocean Modelling*, *80*, 10-23. Retrieved from `https://www.sciencedirect.com/science/article/pii/S146350031400064X` doi: https://doi.org/10.1016/j.ocemod.2014.05.001

Sévellec, F., Naveira Garabato, A. C., Brearley, J. A., & Sheen, K. L. (2015). Vertical flow in the Southern Ocean estimated from individual moorings. *Journal of Physical Oceanography*, *45*(9), 2209–2220. doi: 10.1175/JPO-D-14-0065.1

Stommel, H., & Arons, A. B. (1959). On the abyssal circulation of the world ocean - II. An idealized model of the circulation pattern and amplitude in oceanic basins. *Deep Sea Research (1953)*, *6*(C). doi: 10.1016/0146-6313(59)90075-9

Sugiyama, M. (2016). Chapter 4 - examples of continuous probability distributions. In M. Sugiyama (Ed.), *Introduction to statistical machine learning* (p. 37-50). Boston: Morgan Kaufmann. doi: https://doi.org/10.1016/B978-0-12-802121-7.00015-7

Sverdrup, H. U. (1947). Wind-driven currents in a baroclinic ocean; with application to the equatorial currents of the eastern pacific. *Proceedings of the National Academy of Sciences*, *33*(11), 318–326. Retrieved from `https://www.pnas.org/content/33/11/318` doi: 10.1073/pnas.33.11.318

Swift, D., & Riser, S. (1994, 08). Rafos floats: Defining and targeting surfaces of neutral buoyancy. *Journal of Atmospheric and Oceanic Technology - J ATMOS OCEAN TECHNOL*, *11*, 1079-1092. doi: 10.1175/1520-0426(1994)011⟨1079:RFDATS⟩2.0.CO;2

Tamsitt, V., Drake, H. F., Morrison, A. K., Talley, L. D., Dufour, C. O., Gray, A. R., ... others (2017). Spiraling pathways of global deep waters to the surface of the southern ocean. *Nature communications*, *8*(1), 1–10.

Wang, T., Gille, S. T., Mazloff, M. R., Zilberman, N. V., & Du, Y. (2020). Eddy-induced acceleration of argo floats. *Journal of Geophysical Research: Oceans*, *125*(10), e2019JC016042.

Wong, A. P., Wijffels, S. E., Riser, S. C., Pouliquen, S., Hosoda, S., Roemmich, D., ... Park, H. M. (2020). Argo Data 1999–2019: Two Million Temperature-Salinity Profiles and Subsurface Velocity Observations From a Global Array of Profiling Floats. *Frontiers in Marine Science*, *7*(September), 1–23. doi: 10.3389/fmars.2020.00700

Zilberman, N., Scanderbeg, M., Gray, A., & Oke, P. (2023). Scripps argo trajectory-based velocity product: Global estimates of absolute velocity derived from core, biogeochemical, and deep argo float trajectories at parking depth. *Journal of Atmospheric and Oceanic Technology*.